

Habit-Dependent Vapor Growth Modulates Arctic Supercooled Water Occurrence

Israel Silber¹, Paul S. McGlynn^{1,*}, Jerry Y. Harrington¹, and Johannes Verlinde¹

[1] Department of Meteorology and Atmospheric Science, Pennsylvania State University, University

Park, Pennsylvania, USA

[*] Now at Department of Atmospheric Sciences, University of Utah, Salt Lake City, Utah, USA

Correspondence to: Israel Silber (israel0silber@gmail.com)

April 2021

Ney Points

- The probability of finding topmost supercooled water layers given cloud temperature, P(L/T), provides an impartial water occurrence metric
- P(L/T) using long-term Arctic-site data shows a significant (>20%) ice habit growth impact on liquid occurrence (supported by simulations)
- P(L/T) datasets can provide strong observational targets for models; an example parametrization

for the NSA is provided

This article has been accepted for publication and undergone full peer review but has not been through the copyediting, typesetting, pagination and proofreading process, which may lead to differences between this version and the Version of Record. Please cite this article as doi: 10.1029/2021GL092767.

Abstract

We present an analysis of long-term data collected at Utqiagvik, Alaska, to explore the impacts of cloud processes on the probability of finding supercooled water given cloud temperature, P(L/T), in the topmost unseeded liquid-bearing layers. P(L/T) has local minima at temperatures around -6 °C and -15 °C. Simulations using habit-evolving ice microphysics models suggest that these minima are the result of efficient vapor growth by non-isometric habits found at these temperatures. We conclude that habit-dependent vapor growth of ice crystals modulates the macrophysical occurrence of supercooled water in polar clouds, the effect of which should be included in model parametrizations to avoid biases and/or error compensation. Our methodology is adaptable for spherical ice treatments implemented in models (example parametrizations provided), amenable for use with satellite measurements to give global impartial observational targets for model evaluations, and may allow empirical characterization of bulk responses to seeding and possibly secondary ice effects.

Plain Language Summary

Clouds are responsible for the highest uncertainty in climate model predictions, partially due to deficiencies in the representation of processes controlling the temperature-dependent cloud water phase, and hence, cloud impact on radiative transfer through the atmosphere. Here, we use long-term measurements collected at Utqiagʻvik, Alaska to examine the probability of occurrence of liquid water clouds at a range of sub-freezing temperatures (supercooled clouds). Our methodology allows the robust characterization of occurrence of the highest supercooled cloud per measured atmospheric profile. The resultant probability enables the identification of processes affecting liquid water desiccation. An ensemble of model simulations indicates that significantly lower occurrence of supercooled clouds (by more than 20%) around certain temperatures is the result of the shape and associated rapid growth of precipitating ice crystals formed in these clouds. These fast-growing ice crystals can dry their parent clouds' environment, occasionally resulting in cloud dissipation. We conclude that parametrization of these ice crystal growth rate effects should be included in large-scale models to better represent polar clouds. We also suggest that our method could be easily adapted for satellite measurements to provide a valuable observational database of global supercooled cloud occurrence.

1. Introduction

The relative importance of the physical mechanisms responsible for the observed accelerated warming and greater variability of Arctic surface air temperatures, referred to as Arctic amplification (e.g., Serreze & Barry, 2011), is still not fully understood (e.g., Tan & Storelvmo, 2019). Much of the uncertainty derives from non-linear feedback mechanisms involving meridional transport of heat and moisture, ice-covered surfaces, and cloud processes, all of which impact the surface energy budget (Kay & Gettelman, 2009; Tan & Storelvmo, 2019).

Atmospheric water in all three phases is an important regulator of the Arctic surface energy budget through its contribution to downwelling longwave irradiance (e.g., Curry et al., 1995; Curry & Ebert, 1992; Doyle et al., 2011; Sokolowsky et al., 2020), and as a result of the typical dominance of surface longwave over shortwave radiation at high latitudes (e.g., Shupe & Intrieri, 2004; Turner et al., 2018). The magnitude of downwelling irradiances is modulated by the vertical distribution of water induced by clouds and precipitation, which changes the temperature and density of the emitting water, and hence, the atmospheric emissivity profiles. The dominant phase determining downwelling irradiances varies with season and synoptic conditions. Assuming that a model has the correct total water amount at a given location, how that water is phase partitioned is controlled by in-cloud processes and precipitation below the cloud, emphasizing the need to understand the dominant microphysical processes in polar clouds.

Tan and Storelvmo (2019) explored the effects of modifying the water phase partitioning on Arctic amplification in the CAM5 climate model while constraining the model to satellite-observed condensed phase partitions at different sub-freezing temperatures. Model simulations with modified microphysical scheme parameters resulted in enhanced or reduced Arctic amplification, depending on how the model responded in distributing water through the atmosphere. Middlemas et al. (2020), using the same climate model but with cloud radiative feedbacks disabled ("cloud locking" technique), found

that cloud feedbacks have a negligible influence on Arctic amplification. Both of these studies concluded that the representation of cloud processes, particularly those affecting the supercooled water fraction underestimation in high-latitude clouds, should be a priority if the community is to improve our understanding of the relative importance of the mechanisms driving Arctic amplification. These conclusions are emphasized by recent results (Zelinka et al., 2020) showing that even the latest generation of climate models produce higher and more variable climate sensitivity, which is strongly influenced by the representation of clouds.

Our understanding of the importance of various cloud processes is guided by their signatures in field measurement metrics, such as water phase partitioning. Yet, phase partitioning retrievals are often impacted by unaccounted local influences, as well as non-symmetric instrument sensitivities at detecting ice and liquid hydrometeors. Moreover, because at temperatures below 0 °C greater mass, volume, and/or frequency of ice directly increase its relative fraction, while potentially indirectly decrease the fraction of liquid via accretion and/or desiccation, phase ratio statistics are susceptible to "double-counting" ice-related effects.

In this study, using long-term ground-based observations from Utqiagvik, North Slope of Alaska (NSA; 71.32°N, 156.61°W; Verlinde et al., 2016), we introduce an impartial metric, namely, the conditional probability to detect liquid water given temperature P(L/T) in unseeded topmost cloud layers. Even though this metric does not include explicit information about the presence of ice, the shape of its distribution indicates active primary-ice processes such as nucleation and growth. We examine these indications using parcel and one-dimensional (single-column) model simulations and discuss the results and implications of our analysis on efforts to constrain models.

2. Observed P(L/T) Distribution

To detect liquid-bearing clouds, we use sounding measurements (Holdridge et al., 2011) collected over 7.5 years from November 2011 to April 2019 at Utqiagvik. Liquid-bearing cloud layers

are identified where the measured relative humidity (RH), linearly interpolated onto a 15 m vertical grid spacing, exceeds 95%, which considers the instrument measurement uncertainty. This method for liquid-bearing cloud detection was validated using the same dataset against high spectral resolution lidar phase retrievals (Silber et al., 2020b, fig. S1).

In each of the 8,276 sounding profiles with valid RH measurements, we examine measurements up to the lowest height with temperature less than –40 °C. To minimize seeding effects on our statistics, we only retain data from the topmost liquid-bearing cloud layer in each profile that do not have hydrometeors detected within 60 m above cloud top (see Appendix A). This 60 m criterion also mitigates the influence of secondary ice production (SIP) mechanisms associated with fast falling ice and/or large drops, the general contribution of which to the total number of SIP events is still under active debate (e.g., Field et al., 2017; Korolev & Leisner, 2020; Luke et al., 2021). A cloud is flagged as "seeded" if, in any range gate within these 60 m, Ka-band ARM zenith radar (KAZR; Widener et al., 2012) echoes exist in at least 50% of the 2 s resolution measurements within 15 min after the radiosonde release time (see Silber et al., 2018, 2021). KAZR data are interpolated to the same 15 m vertical grid spacing as sounding data before use. The small allowance for KAZR hydrometeor detections above liquid cloud top considers the horizontal offset between the probed KAZR and sounding air volumes (not shown). Liquid-bearing clouds with tops below the lowest KAZR range gate (ranging from 165 to 225 m above ground level) are excluded from this analysis.

The implementation of these filtering steps enables the principal isolation of primary-ice generating cloud layers, and hence, the implicit consideration of primary-ice nucleation, growth, and sedimentation on the parent clouds. The filtered dataset contains 4,410 profiles, which yields the distribution of the conditional probability for topmost unseeded liquid given temperature P(L/T) by dividing all liquid occurrences per 1 °C temperature interval by the number of occurrences of temperatures within the same interval.

The resultant P(L/T) distribution (Figure 1) depicts an intriguing pattern. The probability values start to increase at a temperature of -36 °C, the lowest temperature at which we reliably detect liquid water occurrence in this dataset. A local minimum and a plateau are observed centering at -15 °C and -6 °C, respectively. These deviations from a generally expected increase in liquid occurrence with temperature, due to decreasing activation of primary ice-nucleating particles (INP; Kanji et al., 2017; Knopf et al., 2018), indicate that other cloud processes impact the liquid water occurrence at these temperatures. We postulate that these observed signatures stem from the amplified vapor depositional growth that occurs near -15 °C and -6 °C due to ice habit (Fukuta & Takahashi, 1999). Dendritic and needle crystals at these respective temperatures grow rapidly (Chen & Lamb, 1994) and thereby reduce liquid water occurrence (Wegener-Bergeron-Findeisen process).

3. Modeling Support for Ice Habit Growth Impact on Liquid Water Occurrence

To investigate our postulated mechanism, we perform parcel model simulations using spherically-shaped and habit-evolving (spheroidal) ice microphysics schemes. The parcel model (Sulia & Harrington, 2011) uses a Lagrangian bin microphysics scheme with spherical and habit-evolving ice treatment (Harrington et al., 2013b). The model is initialized with a specified maximum vertical motion, and temperature, pressure (900 hPa), and RH (95%) representing conditions just below cloud base. The liquid microphysics is initialized with a lognormal distribution of cloud condensation nuclei (CCN) at their equilibrium size (following Feingold & Chuang, 2002) and a concentration of 50 cm⁻³ (see Text S1). Ice is nucleated instantaneously, is initially spherical, and conforms to a gamma size distribution based on a given INP concentration (Harrington et al., 2013b). Ice habits develop following the theory of Chen and Lamb (1994), which models habit evolution with a temperature-dependent inherent growth ratio (IGR). The IGR is defined as the ratio of the basal to the prism face growth rate, and it is a measured quantity. Spherical growth is modeled with an IGR of unity, whereas IGR < 1 (IGR > 1) produces planar (columnar) crystals. The parcel motion follows a sinusoidal pattern

over a fixed depth (400 m) while tracking the microphysics without particle fallout (see also Korolev & Isaac, 2003).

The model is used to calculate liquid water mixing ratio (q_{liq}) and liquid water decay rate (τ_{decay}) within mixed-phase clouds (subfreezing temperatures) in an ensemble of simulations. The ensemble is composed of simulations initialized with 10 different values of INP concentration between 0.1 – $10.0 \, \text{L}^{-1}$ (spaced logarithmically), 17 temperatures between -20 °C and -4 °C (1 °C increments), and 5 maximum vertical velocities between $0.5 - 2.5 \, \text{m/s}$ in $0.5 \, \text{m/s}$ increments, resulting in 850 simulations each for spherical and habit-evolving ice microphysics. The range of these parameters is consistent with measurements over the NSA during the Mixed-Phase Arctic Cloud Experiment (M-PACE; Verlinde et al., 2007), the Indirect and Semi-Direct Aerosol Campaign (ISDAC; McFarquhar et al., 2011), as well as long-term statistics at that site, mainly around autumn (e.g., Lubin et al., 2020; Shupe, 2011)

The example simulation output in Figure 2a demonstrates the impact of the oscillatory parcel motion on the $q_{\rm liq}$ increase and decrease. Because ice particles remain in the parcel (no fallout), the ice particles grow between consecutive cycles, evident by the general increase in ice mixing ratio ($q_{\rm ice}$), while a rather moderate decrease in size is observed during parcel descent of each cycle. The persistently increasing ice particle surface area produces a greater depositional flux of vapor, which reduces the vapor availability for the liquid phase, resulting in stronger evaporation and a decrease in $q_{\rm liq}$ peak near the node of each oscillation. It is arguably the continuous erosion of the peak in $q_{\rm liq}$ that describes the strength of the simulated cloud desiccation, and this can be quantified with a decay time-scale ($\tau_{\rm decay}$), determined by calculating the time it takes for $q_{\rm fiq}$ to fall to 90% of its global maximum value. This moderate decrease threshold enables a $\tau_{\rm decay}$ value to be calculated in all simulations including those initialized with diminished activatable INP concentrations resulting in relatively high global minimum $q_{\rm liq}$ peak value. The $\tau_{\rm decay}$ is computed per simulation by fitting a polynomial curve to the local $q_{\rm liq}$ maxima (gray curve in Figure 2a).

Comparison between the spherical and habit-evolving ice ensembles illustrates the impact of habit growth under different model initializations (Figure 2b). While in spherical ice simulations τ_{decay} decreases commensurately with temperature, habit-evolving simulations using the same model initialization show distinct local τ_{decay} minima at mean parcel temperatures corresponding to dendritic and needle growth (respectively, -15 °C and -7 °C; Bailey & Hallett, 2009). At these temperatures, the IGR reaches its lowest and highest values, respectively, thus promoting strong dendritic and needle growth. The rapid depositional growth of these crystals could generally drain available water molecules faster, and hence, augment liquid phase evaporation. Ice growth patterns at temperatures closer to -10 °C, where the IGR \approx 1, result in more isometric ice particles (e.g., Fukuta & Takahashi, 1999), and hence, the τ_{decay} difference between the spherical and habit-evolving ice simulations minimizes (see Figure 2b).

Even though the parcel model represents only a limited number of the physical aspects of mixed-phase cloud processes, it produces similar patterns to the observational P(L/T) analysis. To show that the parcel model results are not a consequence of the simplified framework, we also examine a smaller ensemble of one-dimensional (1D) cloud model simulations. This 1D model (Golaz, 1998; Simpfendoerfer et al., 2019) represents additional cloud-related processes that are missing in the parcel model such as dynamical feedbacks (following Bechtold et al., 1992), radiation (Harrington, 1997), and particle sedimentation. The model includes a bulk 2-moment version of the same habit-evolving ice microphysics used in the parcel model (Harrington et al., 2013a) and 1-moment cloud droplet treatment. Primary ice crystal nucleation follows the simplified diagnostic approach of Ovchinnikov et al. (2014), in which INP are activated in liquid-bearing grid cells until a maximum specified ice concentration is reached (see Text S2 for detailed model description).

In the simulations performed here, the model is initialized with the sounding profile used for the ISDAC mixed-phase model intercomparison study (Ovchinnikov et al., 2014). The ice-precipitating supercooled cloud layer was relatively long-lived and had a temperature of about -15 °C,

thus providing contextual similarities to the observational analysis in this study. To conduct simulations at different cloud temperatures we modify the baseline sounding by offsetting the initial potential temperature (θ) profile by $\Delta\theta$ while adjusting the water vapor mixing ratio (q_v) such that the initial RH profile remains the same. We vary $\Delta\theta$ such that the mean cloud temperature in different simulations spans a range between -4 °C and -20 °C, while the diagnostic INP concentration is initialized at 9 arbitrarily-selected values ranging from 0.1 - 30 L⁻¹. The CCN number concentration is fixed at 50 cm⁻³ while aggregation processes are turned off.

Unlike the parcel model, liquid-bearing clouds formed in a 1D model simulation have a more complex evolution and may dissipate or persist through the 8-h simulation time. Therefore, applying the $\tau_{\rm decay}$ approach to the 1D model simulations is not straightforward. Instead, we use a different statistic, namely, the q_{liq} relative occurrence fraction. We define the q_{liq} relative fraction as the ratio of the number of liquid-bearing grid cells ($q_{liq} \ge 10^{-4}$ g/kg; e.g., Figure 2c) throughout a simulation to the sum of all model grid cells until cloud dissipation time or the end of the simulation (the earlier of the two).

Similar to the parcel model, the 1D simulation ensemble output shows a distinct habit impact on liquid-bearing cloud occurrence relative to spherical ice treatment (Figure 2d). For simulations with spherical ice, the q_{liq} relative fraction decreases commensurately with temperature. In contrast, the habit-evolving simulations exhibit distinctive valleys centered at mean cloud temperatures of -15 °C and -7 °C. These results indicate that the parcel model agreement with the observations is not the result of its simplified framework.

Taken together, the 1D and parcel model results suggest that the minima in the observed P(L/T) distribution may be due to habit-dependent growth.

4. Discussion

We presented the probability of detecting topmost unseeded liquid cloud layers given temperature P(L/T). A common problem in constraining model simulations using observational targets based on field and satellite measurements is that bulk statistics are often "contaminated" by multiple active processes such as seeding, riming, and SIP, which predominantly require fast falling ice particles and large droplets (e.g., Jensen & Harrington, 2015; Korolev et al., 2020; Korolev & Leisner, 2020). Here we were able to mitigate this "contamination" of liquid-bearing cloud observations by isolating the topmost and unseeded liquid layers, evident by the different P(L/T) distributions generated using all detected liquid-bearing cloud layers or by including seeded cloud layers (see Appendix A). The topmost unseeded P(L/T) distribution (Figure 1) provides a clear indication of ice habit vapor growth on supercooled water occurrence in long-term field observations.

Analyses reported in the literature do provide some indications for habit growth impact on water phase occurrence statistics, mainly around -15 °C (e.g., Hu et al., 2010; Nomokonova et al., 2019; Shupe, 2011; Silber et al., 2020a; Wang et al., 2018; Zhang et al., 2019). In these cases, the analysis often incorporates full datasets without explicit isolation of certain ice-related processes (as in Figure A1), and/or the probability density function of temperature given liquid, P(T/L), and/or a combination of liquid and ice occurrences (phase ratios). Phase ratios derived from single or multiple remote-sensing instruments suffer from instrument detectability limitations (e.g., full attenuation of lidar signals in liquid-bearing clouds, stronger ice radar reflectivity in the dendritic-dominated temperature regime). P(T/L) statistics or statistics calculated without explicit dataset filtering may inextricably convolve spatial and temporal water occurrence variability in the reported values and distributions. Therefore, such statistics are often biased and introduce difficulties in performing direct comparisons with other observational or model output datasets of liquid water occurrence. Moreover, the ice habit-dominated regimes around -15 °C and -6 °C impact both liquid and ice occurrences, thus emphasizing "double counting" biases in phase ratio statistics. This potential for "double counting"

ice effects, a result of liquid and ice process co-dependencies, suggests that the evaluation of liquid water and ice occurrence statistics in observations and models should be performed separately.

P(L/T) of the topmost unseeded cloud layers serves as an impartial statistic with absolute values that are comparable to other dataset statistics calculated following the same methodology. The topmost unseeded liquid-bearing layers' subset required in this methodology can be easily isolated in datasets from spaceborne instruments such as the Cloud-Aerosol Lidar with Orthogonal Polarization (CALIOP; Winker et al., 2003). Therefore, coordinate-dependent P(L/T) can be estimated using satellite observations and reanalysis temperature data and serve as a robust observational target for large-scale model evaluation spanning both supercooled and warm clouds. From a contextual physical perspective, statistics based on unseeded cloud layers essentially incorporate only primary ice-related processes (e.g., Zhang et al., 2018), and hence, are particularly valuable to most current generation large-scale models, which either lack or have a deficient representation of SIP (e.g., Field et al., 2017; Sotiropoulou et al., 2021)

Because most large-scale models including the latest generation climate model sub-group do not include habit-evolving or habit-dependent microphysics, the ice habit signature in the observed P(L/T) imposes an observational constraint that cannot be reproduced by these models without error compensation. To address this issue and thereby provide an observational constraint that is generally reproducible, supported by the parcel and 1D modeling results (Figure 2), we fit a 6th order polynomial to the observed P(L/T) using data points (purple markers in Figure 1) corresponding to temperatures at which more isometric ice particles typically develop (e.g., Bailey & Hallett, 2009). Using this approach, we estimate the P(L/T) that is consistent with the spherical particle assumption common to many models, which is described by

(1)
$$P(L|T)|_{spheres} = -8.494 \cdot 10^{-10} \, T^6 - 1.055 \cdot 10^{-7} \, T^5 - 5.022 \cdot 10^{-6} \, T^4 - 1.126 \cdot 10^{-4} \, T^3 - 1.130 \cdot 10^{-3} \, T^2 - 1.648 \cdot 10^{-3} \, T^1 + 0.05354,$$

where T is in °C (purple curve in Figure 2). We argue that this fitted $P(L/T)|_{spheres}$ can serve as an observational target for large-scale model evaluation using coordinates corresponding to the NSA (how representative this distribution is to other locations should be examined but is beyond the scope of this study).

To estimate the habit impact on the P(L/T) distribution, we separately fit two Gaussians to the residual set of points (at temperatures corresponding to the green markers in Figure 1) after subtracting the observed P(L/T) curve from the polynomial fit (μ_I = -4.789, σ_I = 2.699, A_I = 0.01047, μ_2 = -14.12, σ_2 = 2.708, A_2 = 0.004386; A_i is the normalization factor in units of °C⁻¹). As seen in Figure 1, the polynomial minus two Gaussian fits (green curve) represents more than 99% of the information in the P(L/T) distribution. The magnitude difference of the habit-included fit relative to the spherical-ice estimated fit (Figure 2e) shows that ice shape effects are directly responsible for more than 20% of supercooled water deficit in habit-dominated temperature regimes, in agreement with the modeling results. This observed habit growth magnitude is significantly smaller than the parcel model output around -15 °C, likely because particle fallout is not included.

The observed ice-habit impact on the P(L/T) distribution could theoretically arise from processes not represented in the parcel and 1D models (e.g., large-scale advection, surface heterogeneity, detailed turbulence treatment). Yet, the impact of such processes must systematically occur around -15 °C and -6 °C and not at other temperatures. Assuming, for discussion purposes, that our seeded cloud filtering leaves a significant amount of unfiltered SIP effects in the data subset, the -6 °C minimum could be amplified by these SIP signatures. SIP could also occur at -15 °C, but then a less well-observed process than dendritic growth needs to be postulated (e.g., Field et al., 2017; Korolev & Leisner, 2020). Altogether, currently the simplest most likely explanation for the P(L/T) distribution shape is habit growth effects.

5. Summary

The probability for detecting liquid water in topmost unseeded cloud layers given temperature, P(L/T), can serve as a robust observational metric. The utilization of this metric precludes overweighting ice effects (e.g., via "double counting" in the case of phase ratios) yet still emphasizes the impact of ice nucleation and growth on supercooled water occurrence, as also indicated by model simulation ensembles. The observational and modeling results indicate that primary ice habit effects can diminish supercooled water occurrence by a few tens of percent on first order, and hence, need to be implemented in microphysics schemes to properly represent cloud processes without introducing error compensation and/or biases impacting model evaluation using observations. Knowing that habitevolving microphysics schemes are not on the near horizon for the bulk of large-scale models, we provided a framework to use P(L/T) statistics as observational targets for such models (e.g., climate models). This framework might also fit models that already include some SIP parametrization (see Appendix A). The methodology applied in this study can be easily adapted to satellite measurements, and ultimately, provide local and/or regionally integrated P(L/T) distributions, which could be adjusted for spherical ice implemented in most models. These distributions will offer strong observational benchmarks for large-scale model evaluation from subfreezing to warm temperatures, which are not limited to polar latitudes. We propose that our methodology produces robust liquid occurrence statistics, needed because the community currently lacks comprehensive observational datasets of global water phase mass distribution.

Appendix A: Impact of Seeding on P(L/T)

Figure A1 depicts P(L/T) distributions based on all detected supercooled cloud layers, the topmost detected layers, and the topmost detected layers while excluding seeded clouds. With all detected layers included, the local P(L/T) minimum at -15 °C is relatively shallow while the P(L/T) plateau observed in the topmost unseeded layers' distribution (same as Figure 1) is obscured by

numerous supercooled water detections (e.g., seeded and/or embedded layers) forming a steep P(L/T) slope. These detections also obscure seeding effects that are observed in the distribution using all topmost layers (Figure A1a). When all (seeded and unseeded) topmost cloud layers are compared with the topmost unseeded layers, indications of riming effects on habit growth become discernable, mainly in the normalized distributions (Figure A1b). The distribution based on all topmost layers shows a slightly shallower local minimum around -15 °C relative to the unseeded layer distribution, consistent with reduced habit-induced ice mass vapor growth as a result of riming (relative to unrimed ice; see Jensen & Harrington, 2015). Riming-induced effects are also visible around -5 °C, where occasional SIP likely impacts supercooled cloud properties, resulting in a deep local minimum in the P(L/T) distribution. This potential SIP influence on P(L/T) is centered at a slightly higher temperature relative to the habit growth plateau seen in the unseeded case. Taken together, the comparison between the three distributions suggests that the methodology implemented in this study can mitigate riming-induced effects on the P(L/T) distribution and largely isolates primary from secondary ice effects on supercooled water occurrence.

We note that our fitting methodology (Section 4) can generally be applied on the data subset containing all topmost layers, for example, the two curves in Figure A1a. The purple curve shows a rough estimate for spherical ice calculated by adding the unseeded subset's habit Gaussian fits to the green curve. However, we recommend using fits for such subsets with caution, due to the perplexing entanglement of confounding factors; that is, seeding and SIP effects.

Acknowledgments

The observational data used in this study are available in the ARM data archive (http://www.archive.arm.gov). The observational analysis results and model simulation output illustrated and discussed in the text are available in the Mendeley Data depository under doi:10.17632/6674fwhhtg.2. I.S. is supported by DOE grants DE-SC0018046 and DE-SC0021004.

P.M. and J.Y.H. are grateful for support from the National Science Foundation through Grant AGS-1824243.

6. References

- Bailey, M. P., & Hallett, J. (2009). A Comprehensive Habit Diagram for Atmospheric Ice Crystals:

 Confirmation from the Laboratory, AIRS II, and Other Field Studies. *Journal of the Atmospheric Sciences*, 66(9), 2888–2899. https://doi.org/10.1175/2009JAS2883.1
- Bechtold, P., Pinty, J. P., & Fravalo, C. (1992). A Model of Marine Boundary-Layer Cloudiness for Mesoscale Applications. *Journal of Atmospheric Sciences*, 49(18), 1723–1744. https://doi.org/10.1175/1520-0469(1992)049<1723:AMOMBL>2.0.CO;2
- Chen, J.-P., & Lamb, D. (1994). The Theoretical Basis for the Parameterization of Ice Crystal Habits:

 Growth by Vapor Deposition. *Journal of Atmospheric Sciences*, 51(9), 1206–1222.

 https://doi.org/10.1175/1520-0469(1994)051<1206:TTBFTP>2.0.CO;2
- Curry, J. A., & Ebert, E. E. (1992). Annual Cycle of Radiation Fluxes over the Arctic Ocean:

 Sensitivity to Cloud Optical Properties. *Journal of Climate*, 5(11), 1267–1280.

 https://doi.org/10.1175/1520-0442(1992)005<1267:ACORFO>2.0.CO;2
- Curry, J. A., Schramm, J. L., & Ebert, E. E. (1995). Sea Ice-Albedo Climate Feedback Mechanism.

 **Journal of Climate*, 8(2), 240–247. https://doi.org/10.1175/1520-0442(1995)008<0240:SIACFM>2.0.CO;2
- Doyle, J. G., Lesins, G., Thackray, C. P., Perro, C., Nott, G. J., Duck, T. J., et al. (2011). Water vapor intrusions into the High Arctic during winter. *Geophysical Research Letters*, 38(12). https://doi.org/https://doi.org/10.1029/2011GL047493
- Feingold, G., & Chuang, P. Y. (2002). Analysis of the Influence of Film-Forming Compounds on Droplet Growth: Implications for Cloud Microphysical Processes and Climate. *Journal of the Atmospheric Sciences*, 59(12), 2006–2018. https://doi.org/10.1175/1520-0469(2002)059<2006:AOTIOF>2.0.CO;2

Fuk

- Field, P. R., Lawson, R. P., Brown, P. R. A., Lloyd, G., Westbrook, C., Moisseev, D., et al. (2017).

 Secondary Ice Production: Current State of the Science and Recommendations for the Future.

 Meteorological Monographs, 58, 7.1-7.20. https://doi.org/10.1175/AMSMONOGRAPHS-D-16-0014.1
- Fukuta, N., & Takahashi, T. (1999). The Growth of Atmospheric Ice Crystals: A Summary of Findings in Vertical Supercooled Cloud Tunnel Studies. *Journal of the Atmospheric Sciences*, *56*(12), 1963–1979. https://doi.org/10.1175/1520-0469(1999)056<1963:TGOAIC>2.0.CO;2
- Golaz, J.-C. (1998). Development of a single-column model for simulating precipitating stratocumulus clouds. Colorado State University.
- Harrington, J. Y. (1997). The effects of radiative and microphysical processes on simulated warm and transition season Arctic stratus. Colorado State University.
- Harrington, J. Y., Sulia, K., & Morrison, H. (2013a). A Method for Adaptive Habit Prediction in Bulk Microphysical Models. Part I: Theoretical Development. *Journal of the Atmospheric Sciences*, 70(2), 349–364. https://doi.org/10.1175/JAS-D-12-040.1
- Harrington, J. Y., Sulia, K., & Morrison, H. (2013b). A Method for Adaptive Habit Prediction in Bulk Microphysical Models. Part II: Parcel Model Corroboration. *Journal of the Atmospheric Sciences*, 70(2), 365–376. https://doi.org/10.1175/JAS-D-12-0152.1
- Holdridge, D., Ritsche, M., Prell, J., & Coulter, R. (2011). *Balloon-Borne Sounding System (SONDE)*Handbook. ARM-TR-029, DOE Office of Science, Office of Biological and Environmental Research.
- Hu, Y., Rodier, S., Xu, K., Sun, W., Huang, J., Lin, B., et al. (2010). Occurrence, liquid water content, and fraction of supercooled water clouds from combined CALIOP/IIR/MODIS measurements.

 **Journal of Geophysical Research, 115, D00H34. https://doi.org/10.1029/2009JD012384*
- Jensen, A. A., & Harrington, J. Y. (2015). Modeling Ice Crystal Aspect Ratio Evolution during Riming: A Single-Particle Growth Model. *Journal of the Atmospheric Sciences*, 72(7), 2569–

2590. https://doi.org/10.1175/JAS-D-14-0297.1

- Kanji, Z. A., Ladino, L. A., Wex, H., Boose, Y., Burkert-Kohn, M., Cziczo, D. J., & Krämer, M. (2017). Overview of Ice Nucleating Particles. *Meteorological Monographs*, 58, 1.1-1.33. https://doi.org/10.1175/AMSMONOGRAPHS-D-16-0006.1
- Kay, J. E., & Gettelman, A. (2009). Cloud influence on and response to seasonal Arctic sea ice loss.

 Journal of Geophysical Research: Atmospheres, 114(D18).

 https://doi.org/https://doi.org/10.1029/2009JD011773
- Knopf, D. A., Alpert, P. A., & Wang, B. (2018). The Role of Organic Aerosol in Atmospheric Ice Nucleation: A Review. ACS Earth and Space Chemistry, 2(3), 168–202. https://doi.org/10.1021/acsearthspacechem.7b00120
- Korolev, A., & Isaac, G. (2003). Phase transformation of mixed-phase clouds. *Quarterly Journal of the Royal Meteorological Society*, 129(587), 19–38. https://doi.org/https://doi.org/10.1256/qj.01.203
- Korolev, A., & Leisner, T. (2020). Review of experimental studies of secondary ice production.

 *Atmospheric Chemistry and Physics, 20(20), 11767–11797. https://doi.org/10.5194/acp-20-11767-2020
- Korolev, A., Heckman, I., Wolde, M., Ackerman, A. S., Fridlind, A. M., Ladino, L. A., et al. (2020).

 A new look at the environmental conditions favorable to secondary ice production. *Atmos. Chem. Phys.*, 20(3), 1391–1429. https://doi.org/10.5194/acp-20-1391-2020
- Lubin, D., Zhang, D., Silber, I., Scott, R. C., Kalogeras, P., Battaglia, A., et al. (2020). AWARE: The Atmospheric Radiation Measurement (ARM) West Antarctic Radiation Experiment. *Bulletin of the American Meteorological Society*, *101*(7), E1069–E1091. https://doi.org/10.1175/BAMS-D-18-0278.1
- Luke, E. P., Yang, F., Kollias, P., Vogelmann, A. M., & Maahn, M. (2021). New insights into ice multiplication using remote-sensing observations of slightly supercooled mixed-phase clouds in

the Arctic. *Proceedings of the National Academy of Sciences*, 118(13). https://doi.org/10.1073/pnas.2021387118

McFarquhar, G. M., Ghan, S., Verlinde, J., Korolev, A., Strapp, J. W., Schmid, B., et al. (2011).

Indirect and Semi-direct Aerosol Campaign. *Bulletin of the American Meteorological Society*, 92(2), 183–201. https://doi.org/10.1175/2010BAMS2935.1

Middlemas, E. A., Kay, J. E., Medeiros, B. M., & Maroon, E. A. (2020). Quantifying the Influence of Cloud Radiative Feedbacks on Arctic Surface Warming Using Cloud Locking in an Earth System Model. *Geophysical Research Letters*, 47(15), e2020GL089207. https://doi.org/https://doi.org/10.1029/2020GL089207

Nomokonova, T., Ebell, K., Löhnert, U., Maturilli, M., Ritter, C., & O'Connor, E. (2019). Statistics on clouds and their relation to thermodynamic conditions at Ny-Ålesund using ground-based sensor synergy. *Atmospheric Chemistry and Physics*, 19(6), 4105–4126. https://doi.org/10.5194/acp-19-4105-2019

Ovchinnikov, M., Ackerman, A. S., Avramov, A., Cheng, A., Fan, J., Fridlind, A. M., et al. (2014).

Intercomparison of large-eddy simulations of Arctic mixed-phase clouds: Importance of ice size distribution assumptions. *Journal of Advances in Modeling Earth Systems*, 6(1), 223–248. https://doi.org/10.1002/2013MS000282

Serreze, M. C., & Barry, R. G. (2011). Processes and impacts of Arctic amplification: A research synthesis. *Global and Planetary Change*, 77(1), 85–96. https://doi.org/https://doi.org/10.1016/j.gloplacha.2011.03.004

Shupe, M. D. (2011). Clouds at Arctic Atmospheric Observatories. Part II: Thermodynamic Phase Characteristics. *Journal of Applied Meteorology and Climatology*, 50(3), 645–661. https://doi.org/10.1175/2010JAMC2468.1

Shupe, M. D., & Intrieri, J. M. (2004). Cloud Radiative Forcing of the Arctic Surface: The Influence of Cloud Properties, Surface Albedo, and Solar Zenith Angle. *Journal of Climate*, 17(3), 616–

628. https://doi.org/10.1175/1520-0442(2004)017<0616:CRFOTA>2.0.CO;2

Silber, I., Verlinde, J., Eloranta, E. W., & Cadeddu, M. (2018). Antarctic cloud macrophysical, thermodynamic phase, and atmospheric inversion coupling properties at McMurdo Station. Part I: Principal data processing and climatology. *Journal of Geophysical Research: Atmospheres*. https://doi.org/10.1029/2018JD028279

Silber, I., Verlinde, J., Wen, G., & Eloranta, E. W. (2020a). Can Embedded Liquid Cloud Layer

Volumes Be Classified in Polar Clouds Using a Single-Frequency Zenith-Pointing Radar? *IEEE Geoscience and Remote Sensing Letters*, 17(2), 222–226.

https://doi.org/10.1109/LGRS.2019.2918727

Silber, I., Fridlind, A. M., Verlinde, J., Russell, L. M., & Ackerman, A. S. (2020b). Nonturbulent Liquid-Bearing Polar Clouds: Observed Frequency of Occurrence and Simulated Sensitivity to Gravity Waves. *Geophysical Research Letters*. https://doi.org/10.1029/2020GL087099

Silber, I., Fridlind, A. M., Verlinde, J., Ackerman, A. S., Cesana, G. V., & Knopf, D. A. (2021). The Prevalence of Precipitation from Polar Supercooled Clouds. *Atmos. Chem. Phys.* https://doi.org/10.5194/acp-2020-993

Simpfendoerfer, L. F., Verlinde, J., Harrington, J. Y., Shupe, M. D., Chen, Y.-S., Clothiaux, E. E., & Golaz, J.-C. (2019). Formation of Arctic Stratocumuli Through Atmospheric Radiative Cooling. *Journal of Geophysical Research: Atmospheres*. https://doi.org/10.1029/2018JD030189

Sokolowsky, G. A., Clothiaux, E. E., Baggett, C. F., Lee, S., Feldstein, S. B., Eloranta, E. W., et al. (2020). Contributions to the Surface Downwelling Longwave Irradiance during Arctic Winter at Utqiagʻvik (Barrow) Alaska. *Journal of Climate*. https://doi.org/10.1175/JCLI-D-18-0876.1

Sotiropoulou, G., Vignon, É., Young, G., Morrison, H., O'Shea, S. J., Lachlan-Cope, T., et al. (2021).

Secondary ice production in summer clouds over the Antarctic coast: an underappreciated process in atmospheric models. *Atmospheric Chemistry and Physics*, 21(2), 755–771. https://doi.org/10.5194/acp-21-755-2021

- Sulia, K. J., & Harrington, J. Y. (2011). Ice aspect ratio influences on mixed-phase clouds: Impacts on phase partitioning in parcel models. *Journal of Geophysical Research: Atmospheres*, *116*(D21). https://doi.org/10.1029/2011JD016298
- Tan, I., & Storelvmo, T. (2019). Evidence of Strong Contributions From Mixed-Phase Clouds to Arctic Climate Change. *Geophysical Research Letters*, 46(5), 2894–2902. https://doi.org/10.1029/2018GL081871
- Turner, D. D., Shupe, M. D., & Zwink, A. B. (2018). Characteristic Atmospheric Radiative Heating Rate Profiles in Arctic Clouds as Observed at Barrow, Alaska. *Journal of Applied Meteorology and Climatology*, 57(4), 953–968. https://doi.org/10.1175/JAMC-D-17-0252.1
- Verlinde, J., Harrington, J. Y., Yannuzzi, V. T., Avramov, A., Greenberg, S., Richardson, S. J., et al. (2007). The Mixed-Phase Arctic Cloud Experiment. *Bulletin of the American Meteorological Society*, 88(2), 205–221. https://doi.org/10.1175/BAMS-88-2-205
- Verlinde, J., Zak, B. D., Shupe, M. D., Ivey, M. D., & Stamnes, K. (2016). The ARM North Slope of Alaska (NSA) Sites. *Meteorological Monographs*, 57, 8.1-8.13. https://doi.org/10.1175/AMSMONOGRAPHS-D-15-0023.1
- Wang, Y., Zhang, D., Liu, X., & Wang, Z. (2018). Distinct Contributions of Ice Nucleation, Large-Scale Environment, and Shallow Cumulus Detrainment to Cloud Phase Partitioning With NCAR CAM5. *Journal of Geophysical Research: Atmospheres*, 123(2), 1132–1154. https://doi.org/https://doi.org/10.1002/2017JD027213
- Widener, K. B., Bharadwaj, N., & Johnson, K. (2012). *Ka-Band ARM Zenith Radar (KAZR) Instrument Handbook*. United States: ARM-TR-106, DOE Office of Science, Office of Biological and Environmental Research. https://doi.org/10.2172/1035855
- Winker, D. M., Pelon, J. R., & McCormick, M. P. (2003). The CALIPSO mission: spaceborne lidar for observation of aerosols and clouds (Vol. 4893, pp. 1–11). Retrieved from http://dx.doi.org/10.1117/12.466539

Zelinka, M. D., Myers, T. A., McCoy, D. T., Po-Chedley, S., Caldwell, P. M., Ceppi, P., et al. (2020).

Causes of Higher Climate Sensitivity in CMIP6 Models. *Geophysical Research Letters*, 47(1), e2019GL085782. https://doi.org/https://doi.org/10.1029/2019GL085782

Zhang, D., Wang, Z., Kollias, P., Vogelmann, A. M., Yang, K., & Luo, T. (2018). Ice particle production in mid-level stratiform mixed-phase \hack{\break} clouds observed with collocated A-Train measurements. *Atmospheric Chemistry and Physics*, 18(6), 4317–4327. https://doi.org/10.5194/acp-18-4317-2018

Zhang, D., Vogelmann, A., Kollias, P., Luke, E., Yang, F., Lubin, D., & Wang, Z. (2019). Comparison of Antarctic and Arctic Single-Layer Stratiform Mixed-Phase Cloud Properties Using Ground-Based Remote Sensing Measurements. *Journal of Geophysical Research: Atmospheres*, 124(17–18), 10186–10204. https://doi.org/10.1029/2019JD030673

7. References from the Supporting Information

Bechtold, P., Pinty, J. P., & Fravalo, C. (1992). A Model of Marine Boundary-Layer Cloudiness for Mesoscale Applications. *Journal of Atmospheric Sciences*, 49(18), 1723–1744. https://doi.org/10.1175/1520-0469(1992)049<1723:AMOMBL>2.0.CO;2

Feingold, G., & Chuang, P. Y. (2002). Analysis of the Influence of Film-Forming Compounds on Droplet Growth: Implications for Cloud Microphysical Processes and Climate. *Journal of the Atmospheric Sciences*, 59(12), 2006–2018. https://doi.org/10.1175/1520-0469(2002)059<2006:AOTIOF>2.0.CO;2

Golaz, J.-C. (1998). Development of a single-column model for simulating precipitating stratocumulus clouds. Colorado State University.

Harrington, J. Y. (1997). The effects of radiative and microphysical processes on simulated warm and transition season Arctic stratus. Colorado State University.

Harrington, J. Y., Meyers, M. P., Walko, R. L., & Cotton, W. R. (1995). Parameterization of Ice Crystal

Harri

Conversion Processes Due to Vapor Deposition for Mesoscale Models Using Double-Moment Basis Functions. Part I: Basic Formulation and Parcel Model Results. *Journal of Atmospheric Sciences*, 52(23), 4344–4366. https://doi.org/10.1175/1520-0469(1995)052<4344:POICCP>2.0.CO;2

- Harrington, J. Y., Sulia, K., & Morrison, H. (2013). A Method for Adaptive Habit Prediction in Bulk Microphysical Models. Part I: Theoretical Development. *Journal of the Atmospheric Sciences*, 70(2), 349–364. https://doi.org/10.1175/JAS-D-12-040.1
- Harrington, J. Y., & Olsson, P. Q. (2001). On the potential influence of ice nuclei on surface-forced marine stratocumulus cloud dynamics. *Journal of Geophysical Research: Atmospheres*, 106(D21), 27473–27484. https://doi.org/10.1029/2000JD000236
- Jensen, A. A., Harrington, J. Y., Morrison, H., & Milbrandt, J. A. (2017). Predicting Ice Shape Evolution in a Bulk Microphysics Model. *Journal of the Atmospheric Sciences*, 74(6), 2081–2104. https://doi.org/10.1175/JAS-D-16-0350.1
- Langland, R. H., & Liou, C.-S. (1996). Implementation of an E–ε Parameterization of Vertical Subgrid-Scale Mixing in a Regional Model. *Monthly Weather Review*, 124(5), 905–918. https://doi.org/10.1175/1520-0493(1996)124<0905:IOAPOV>2.0.CO;2
- Lebo, Z. J., Johnson, N. C., & Harrington, J. Y. (2008). Radiative influences on ice crystal and droplet growth within mixed-phase stratus clouds. *Journal of Geophysical Research: Atmospheres*, 113(D9). https://doi.org/https://doi.org/10.1029/2007JD009262
- Meyers, M. P., Walko, R. L., Harrington, J. Y., & Cotton, W. R. (1997). New RAMS cloud microphysics parameterization. Part II: The two-moment scheme. *Atmospheric Research*, 45(1), 3–39. https://doi.org/https://doi.org/10.1016/S0169-8095(97)00018-5
- Ovchinnikov, M., Ackerman, A. S., Avramov, A., Cheng, A., Fan, J., Fridlind, A. M., ... Sulia, K. (2014). Intercomparison of large-eddy simulations of Arctic mixed-phase clouds: Importance of

ice size distribution assumptions. *Journal of Advances in Modeling Earth Systems*, *6*(1), 223–248. https://doi.org/10.1002/2013MS000282

Stull, R. B. (1988). *An introduction to boundary layer meteorology* (Vol. 13). Springer Science & Business Media. https://doi.org/10.1007/978- 94- 009- 3027- 8

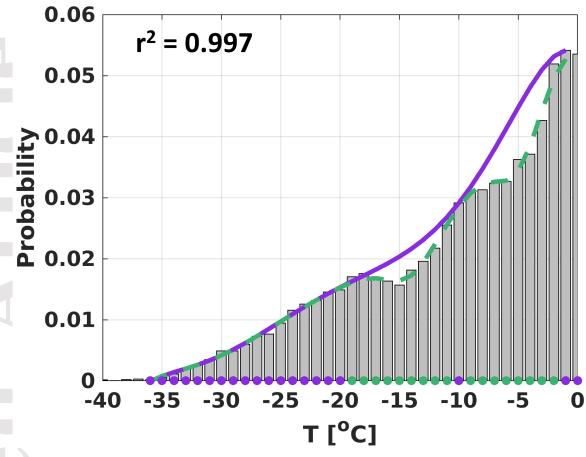
Sulia, K. J., & Harrington, J. Y. (2011). Ice aspect ratio influences on mixed-phase clouds: Impacts on phase partitioning in parcel models. *Journal of Geophysical Research: Atmospheres*, *116*(D21). https://doi.org/10.1029/2011JD016298

List of Figures:

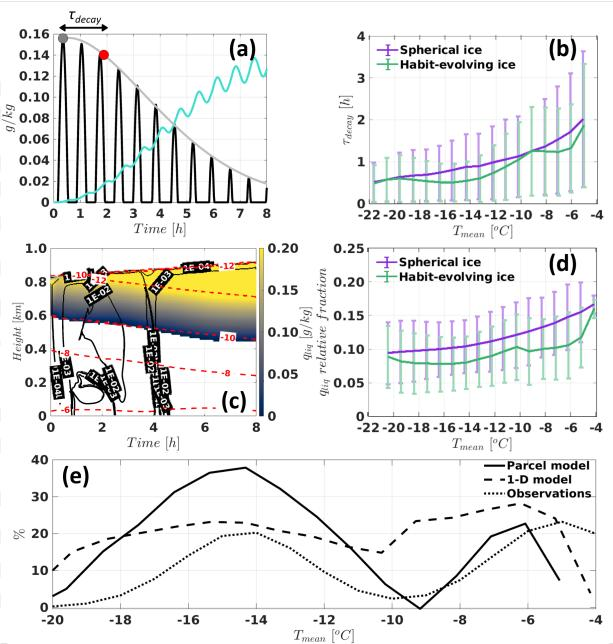
Figure 1: Probability of topmost unseeded liquid given temperature, P(L/T) (bars). The purple curve shows a 6^{th} order polynomial fit using the distribution data points denoted by the purple markers, which represents a qualitative distribution estimate for spheres. The green curve represents a fitted distribution resulting from subtracting two separate Gaussian fits (using the green-color marked data points) for each of the two extreme habit growth regions around -15 and -6 °C from the sphere-estimated curve (see text for details). The coefficient of determination (r^2) for the green curve is shown at the top of the figure.

Figure 2: (a) Parcel model output liquid water (black) and ice (green) mixing ratios (q_{liq} and q_{ice}) using habit-evolving ice microphysics, ice nucleating particle (INP) concentration of 0.1 L⁻¹, initial temperature of -12 °C, and maximum vertical motion of 0.5 m/s. The gray curve illustrates the 6th order polynomial fit to q_{liq} peaks. The gray marker denotes the global q_{liq} maximum, and the red marker designates the time on which the fit's value is 90% of the global maximum, from which the liquid decay time (τ_{decay}) is determined (see text for details). (b) Parcel model simulation ensemble mean τ_{decay} for spherical and habit-evolving ice microphysics (see legend) as a function of mean parcel temperature. The error bars represent the mean $\pm 1\sigma$. (c) Onedimensional model output for habit-evolving ice using a diagnostic INP concentration of 1.0 L⁻¹ and temperature profile offset of 3 °C. The color-scale illustrates q_{liq} while the black (red) contours denote q_{ice} (temperature). (d) As in panel b but showing the one-dimensional model simulation ensemble mean q_{liq} relative occurrence fraction as a function of mean liquid-bearing grid cell temperature. (e) Parcel (one-dimensional) model simulation ensemble mean τ_{decay} (q_{liq} relative fraction) magnitude change in habit-evolving ice simulations relative to spherical ice together with the estimated P(L/T) magnitude changes calculated using the observationallybased fits (see legend and text for details).

Figure A1: (a) P(L/T) distributions based on all detected supercooled cloud layers, the topmost detected layers (per liquid-bearing sounding profile), and the topmost detected layers while excluding seeded cases (see legend). The green curve denotes the combination of a 6^{th} order polynomial and two Gaussian fits to the "topmost layers" distribution ($r^2 = 0.998$; similar to the green curve in Figure 1), and the dashed purple curve shows the spherical ice fit for this subset (see Appendix A). (b) same, but with the two topmost layer distributions normalized such that P(L/T) at -10 °C equals to the full dataset ("all layers") value (dashed black curve designates the obstructed "all layers" bars).









All layers

Topmost layers
Topmost unseeded layers
Polynomial & 2 Gaussian fits
Same + unseeded Gaussian fits

-35 -30 -25 -20 -15

T [°C]

-40

(a)

-10

-5

